Composites Science and Technology 248 (2024) 110439

Contents lists available at ScienceDirect

Composites Science and Technology

journal homepage: www.elsevier.com/locate/compscitech

Bayesian optimization-based prediction of the thermal properties from fatigue test IR imaging of composite coupons

Martin Demleitner [b], Rodrigo Q. Albuquerque [b,c,*], Ali Sarhadi [a,*], Holger Ruckdäschel [b,c,*], Martin A. Eder [a]

[a] Technical University of Denmark, Frederiksborgvej 399, Roskilde 4000, Denmark
[b] University of Bayreuth, Universitätsstrasse 30, Bayreuth 95447, Germany
[c] Neue Materialien Bayreuth GmbH, Gottlieb-Keim-Straße 60, Bayreuth 95448, Germany

ARTICLE INFO

Keywords:
Bayesian optimization
Glass/epoxy composites fatigue testing
Thermal properties
IR imaging

ABSTRACT

The prediction of the prevailing self-heat transfer parameters of a glass/epoxy composite coupon during fatigue testing in general and the distinction between viscoelastic- and frictional crack growth-related energy dissipation in particular, are not trivial problems. This work investigates the feasibility of predicting the convective film coefficient, the total work loss as well as the ratio between viscoelastic and fracture-induced damping from thermal images using Bayesian optimization in conjunction with 3D FE thermal analysis. To this end, glass fiber/epoxy biax coupons are pre-damaged by means of a drop weight impact machine and subsequently tested under uniaxial tension-tension high cycle fatigue conditions. IR images are taken of the self-heating thermal profile at steady-state conditions. Synthetic surface thermal images are generated by numerical thermal analysis of the damage distribution obtained by μ-CT scanning prior to testing. Bayesian optimization of the aforementioned parameters is conducted by minimizing the loss function between the as-measured and the synthetic IR image. The predicted work-loss is consequently validated against the measured hysteretic response, from which a very good agreement is found.

1. Introduction

Despite its significant application to remote structural health monitoring systems [1–3], passive thermography in composites is finding its way into fatigue damage characterization during fatigue tests primarily for the purpose of controlling the self-heating core temperature in the coupons.

Self-heating phenomena are well known to influence the performance of composites [4]. The self-heating behaviour of a fiber/polymer composite material subject to high cycle fatigue is inherently thermodynamically intertwined with the prevailing fatigue damage mechanism — figuratively speaking representing two sides of the same medal. Infrared (IR) thermal images obtained during fatigue tests contain key information about the current damage state and the rate (stage) of the damage evolution [5–7]. Experimental thermal imaging is hence of significant importance for both, experimental and theoretical research, shedding light on the highly complex fatigue damage mechanisms in composites.

Thermography is a widely used and established method for fatigue damage and progress detection of composites, both for glass fiber [8–10] and carbon-fiber reinforced composites [11–13]. Due to the low thermal conductivity of the polymer and especially glass fibers, fast heat-build up is especially visible for thick laminates where the generated heat cannot be released efficiently by convection via the composite surfaces [14,15]. Especially in case of formed defects by impact damage, the resulting hotspot formation and evolution (location and severity) can be detected and traced via thermography during fatigue processes [16–19].

However, two main issues arise when trying to extract useful information from IR images: First, the thermal surface profile is among others, a superposition of heat generated by viscoelastic effects on material scale and frictional effects associated with the defect, especially the crack evolution on meso- and macro scale. Second, the thermal image is the result of a complex anisotropic 3D heat transfer mechanism which hardly allows for a direct interpretation of the true damage size and shape, particularly in the case of sub-surface damage.

Distinguishing viscous dissipation from frictional dissipation and extracting information of the total work loss and the associated damage characteristics usually requires the solution of a thermal model and, in

* Corresponding authors.
E-mail addresses: rodrigo.q.albuquerque@uni-bayreuth.de (R.Q. Albuquerque), asar@dtu.dk (A. Sarhadi), holger.ruckdaeschel@uni-bayreuth.de (H. Ruckdäschel).

https://doi.org/10.1016/j.compscitech.2024.110439
Received 4 October 2023; Received in revised form 15 December 2023; Accepted 10 January 2024
Available online 12 January 2024

a narrower sense, the solution to a thermoelastic problem e.g. demonstrated in the literature [20]. Validating the numerical model predictions against experimental IR imaging requires accurate knowledge of the in-situ heat transfer boundary conditions pertaining to the heat flux between the specimen and the grips as well as the convective heat flux governed by the film coefficient. Particularly the latter has the strongest influence on the surface temperature profile and simultaneously represents arguably the most illusive parameter to determine. This becomes increasingly apposite in thick laminates in which the self-heating occurs deep inside the material. Laminates are generally designated as *'thick'* when their thickness exceeds 6 mm. This becomes particularly pertinent when considering applications such as wind energy rotor blades or tidal blades [21,22]. In these scenarios, the blade tips often boast thicknesses of around 20 mm, while the rotor blade roots can extend to typical dimensions of up to several hundred mm [23]. Several researchers have explored the fatigue behaviour of thick laminates, utilizing thermography methods to gain deeper insights into the material's behaviour [24–29].

Defects especially based on impact and fatigue or a combination of both can have quite complex structure based on cracks, delamination scattered over the whole volume or only certain parts. Depending on the thickness, different defect patterns can occur in laminates: thin ones might exhibit bending cracks over the whole thickness, while thicker ones can show shear-induced delamination in selected plies due to higher bending stiffness [30]. It is important to underscore that beyond laminate thickness, other factors including fiber type, lay-up configuration, and matrix toughness can have a significant influence on defect formation and propagation. Consequently, the precise determination of the true nature of defects can be challenging.

Understanding the unknown conditions and impacts of defects, along with their influence on heat generation and conduction under various boundary conditions, constitutes a significant area of research. Multiple approaches have been pursued in this field, including computational methods [31], Bayesian inference techniques [32], and finite element algorithms [33] all aimed at solving different kinds of inverse heat problems. Recently machine learning techniques evolved, proven themselves superior in finding optimal parameter and detecting correlations in large and complex data sets without the need of explicit mathematical models. There exist several instances showcasing the application of ML models in resolving inverse heat problems and defect detection [34–38]. Especially the ML technique called Bayesian Optimization (BO) has proven effective in reducing the time required to discover optimal parameters in various polymer-related applications [39–41]. The BO technique is an important statistical tool that can help optimize multiple parameters aiming at maximizing or minimizing target properties [42]. For instance, Park et al. [41] have maximized the toughness of polymer-based composites by optimizing two geometrical parameters used to assemble staggered platelet composite structures. Chen et al. [43] used BO to perform an efficient screening of flame retardants for polymer composites. Especially in the case of time-consuming experiments, employing BO to optimize parameters is an elegant solution to address sustainability issues, as it avoids many costly trial-and-error rounds.

One could also optimize parameters leading to desired properties by means of training an accurate ML model using many samples (or data points). In this inverse design approach, also called 'high throughput virtual screening', the trained ML model performs predictions on a representative region of the multidimensional space of parameters to find the best ones leading to the desired target property. For instance, Albuquerque et al. [42] trained a kernel ridge model using 29 samples of seven dimensions each and screened a virtual space of about 10^6 samples to propose six new samples exhibiting a target property in a specific range. In the global optimization category, other algorithms other than BO can also be used, such as the particle swarm optimization or the genetic algorithm. The advantage of BO lies in its efficiency with limited evaluations, adaptability to differentiable and non-differentiable functions, and its robustness to noisy objectives. A good review on different data-driven optimization techniques has been recently published [44].

This sets the incentive for this work, whose purpose is to investigate both, the feasibility and accuracy to predict the following three parameters from experimentally obtained thermal images:

i the equivalent convective film coefficient of the exposed specimen surface
ii the total steady state dissipated energy or hysteretic work loss
iii the estimated relative portion of viscoelastic energy dissipation

These parameters play a pivotal role in precisely forecasting the material's fatigue life, understanding failure mechanisms, and refining the material's design to achieve superior durability and reliability. An accurate prediction of these parameters enables the distinction between viscoelastic heat generation and crack growth induced frictional heat generation ultimately leading to more accurate fatigue life predictions. To this end, the IR images of two specimens with a predefined damage subject to fatigue loading are used to predict the optimal parameter set using BO in conjunction with synthetic thermal images generated by 3D thermal FEA. To the authors best knowledge, this is the first attempt to predict the thermal properties of a glass/epoxy composite coupon subject to fatigue self-heating from IR images using BO, which highlights the novelty and significance and the present work. In addition, this study also contributes to the improvement of the fatigue damage predictions of thermo-elastic models with applications in structural health monitoring and in coupon temperature control during fatigue testing.

2. Materials and methodology

2.1. Specimen preparation and μ-CT

The coupons were manufactured from a biaxial glass fiber epoxy composite material by a resin transfer molding process. A *DGEBA* epoxy resin (DER331) with a *IPDA/Jeffamine D230* (50%/50%) mixture as curing agent was used and injected at room temperature. This resin system is similar to the commonly used resin system *RIMR135* + *RIMH134* for wind rotor blade manufacturing. The glass fiber material was a ±45° Biaxial NCF with an areal weight of 600 g/m^2. The laminate was cured and post cured according to the following curing cycle: 80 °C for 1 h and an additional 1 h at 140 °C. The laminate had a fiber volume content of 60 ± 2% determined by thermogravimetric analysis.

The rectangular nominal geometry adopted here is shown in Fig. 1 (a), which followed the specifications stipulated in DIN ISO 14129 [45] with a total length (L) of 250 mm, a width (W) of 25 mm and a thickness (t) of 6 mm.

Subsequently to manufacturing, a pre-damage was introduced into the gauge region by means of a low-velocity drop weight impact machine *CEAST Fractovis Plus* using a 20 mm diameter impactor with a hemispherical tip. The purpose of the pre-damage was to obtain a clearly defined hotspot location during fatigue testing. Impact energies of 5 J and 10 J were applied which resulted in a trombone-shaped opaque area widening towards the back-side of the coupon whose dimensions are listed in Table 1. Here, D_f is the diameter of the opaque area on the front side and D_b the diameter of the opaque area on the back side. The as-impacted 10 J coupon is shown in Fig. 2(a). 5 J and 10 J impact energies were used to induce adequate damage however without surpassing a threshold where the damage becomes excessively significant, preventing the creation of a stable plateau in the material response during fatigue loading.

The region around the impact was scanned by micro computed tomography using a *phoenix v|tome|xs 240/180* (Baker Hughes Digital Solutions GmbH, Hürth, Germany) with a voxel size of 15 µm. The 3D microcrack distribution identified in the defect analysis appeared to

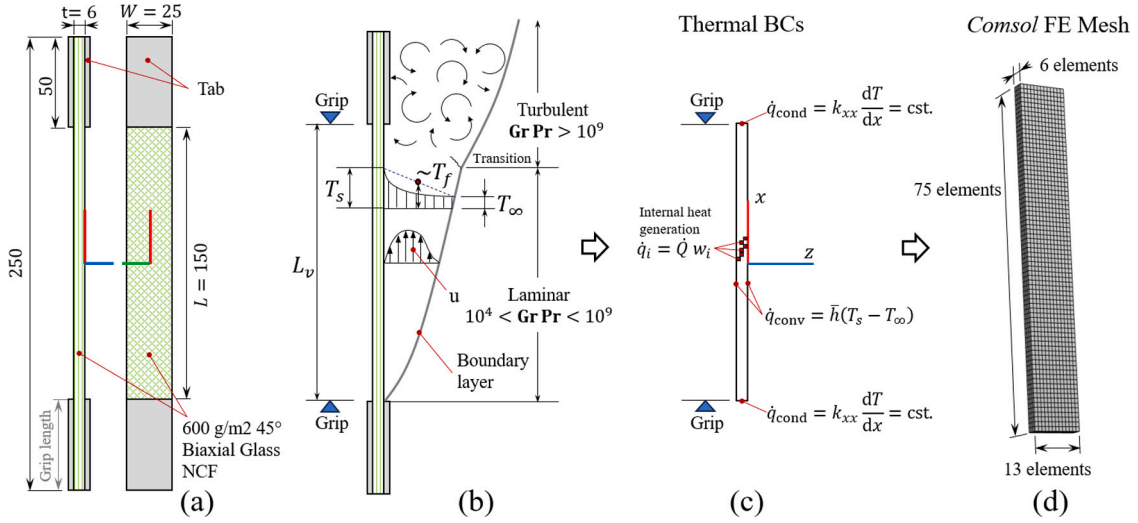

Fig. 1. (a) Geometry of the specimen and (b) schematic depiction of the natural convection conditions with upward velocity field in vicinity of the thin vertical coupon caused by buoyancy forces of the heated air film in close vicinity of the surface; non-linear temperature gradient between the surface and the ambient air; also indicated the transition between laminar and turbulent flow depending on the product of the *Prandtl* and the *Grashof* number bearing high uncertainty and (c) thermal boundary conditions applied to the thermal model with internal heat sources and (d) finite element mesh with discretization levels.

Table 1
Thickness and approximate opaque region diameters obtained from surface inspection of the as-measured coupons.

Energy J	t mm	D_f mm	D_b mm
5	6.4	12	20
10	6.85	13	20

be mostly inter- and intra-laminar delamination preferably occurring around the actual impact site (see the SI) and was saved as unstructured triangulated mesh in *.stl* format. Surprisingly, the opaque impact region was not resolved in the CT data, which is believed to be caused by violent obliteration of the material entailing a homogeneous distribution of microcracks whose characteristic length was smaller than the voxel size. This way, a sufficient contrast between cracks and intact material in the X-ray attenuation pattern was largely prevented in the local impact region.

2.2. Uniaxial high cycle fatigue experiments

After CT scanning, the coupons were tested in a servo-hydraulic uniaxial testing machine (*Schenk, IST 8800/Software Dynmat by BASF AG, Ludwigshafen*) at room temperature, at a constant stress ratio of $R = 0.1$ and at a frequency of 5 Hz with a sinusoidal waveform. The cyclic loading was set to 40 MPa as the upper load level and 4 MPa as the lower load level. These values were chosen based on previously conducted static tensile shear tests as they are well below load levels where interfiber breakage occurs but significant thermal hotspot formation takes place due to friction in the defect zone. Axial strains in the loading direction were measured by a tactile clip extensometer attached to the centre of the gauge zone. A thermal video camera (*VarioCAM hd 980 of InfraTec*) was positioned at a distance of 60 cm to the specimen surface. The frame rate was 30 Hz with a measurement accuracy of ±1.5 K. Prior to testing the specimens were sprayed with a *Black Matt, Duplicolor Acrylat* coating and the emissivity was set to a value of 1. The entire test setup is shown in Fig. 3(a).

The hysteretic energy dissipation cf. Fig. 3(b) was obtained from integrating the measured hysteresis loop of one complete cycle as follows:

$$\omega = f\frac{L\,W\,t}{2}\sum_{k=1}^{m}\left(\sigma_{k+1}+\sigma_k\right)\left(\epsilon_{k+1}-\epsilon_k\right) \quad \text{if } k=m \text{ then } \sigma_{k+1}=\sigma_1 \text{ and } \epsilon_{k+1}=\epsilon_1 \tag{1}$$

f is the test frequency (in Hz), and σ in (MPa) and ϵ are the nominal axial stress and unitless axial engineering strain, respectively. Eq. (1) was evaluated in the clockwise direction for every consecutive timestamp belonging to the set forming one complete load cycle.

2.3. Heat source generation for thermal analysis

Fig. 2(b) shows the distribution of the microcrack vertices which were imported from the μ-CT *.stl* file into a *Matlab* [46] script. An impact microcrack cloud comprising of randomly distributed points inside a through-thickness conical boundary volume defined by D_f, D_s (see Table 1) was added to the CT-scan data cf. Fig. 2(c). The self-heating process of the coupon was simulated by a distributed internal heat source arising from the linear superposition of a viscoelastic and a frictional contribution.

Considering a constant strain rate in the coupon as a first order approximation, the viscoelastic portion is equally assumed to be constant and stipulated as the unitless scalar η. Conversely, the frictional portion induced by the microcracks is represented by the point cloud distribution where it is hypothesized that the heat induced in an arbitrary finite control volume is directly proportional to the number of cracks contained within. Following this hypothesis, the point cloud in the analysis domain was binned into equally sized cuboid control volumes whose dimensions correspond to the finite element size. Fig. 2(d) shows that the domain was discretized into $N = 75 \times 13 \times 6 = 5850$ elements into which the points have been binned according to the algorithm 1.

Eq. (2) shows the weight calculated for each element depicted in the colour contour plot of Fig. 2(d). Each unitless weight representing the intensity of heat influx consists of a viscoelastic part w_i^V and a crack contribution w_i^G. In the former, η is distributed equally over N and the latter uses the information of the points per element matrix (n) obtained from the algorithm 1 normalized against the total number of points k. Eq. (3) shows that the sum of all weights must be one.

$$w_i = w_i^V + w_i^G = \frac{\eta}{N} + (1-\eta)\,\frac{n_i}{k} \tag{2}$$

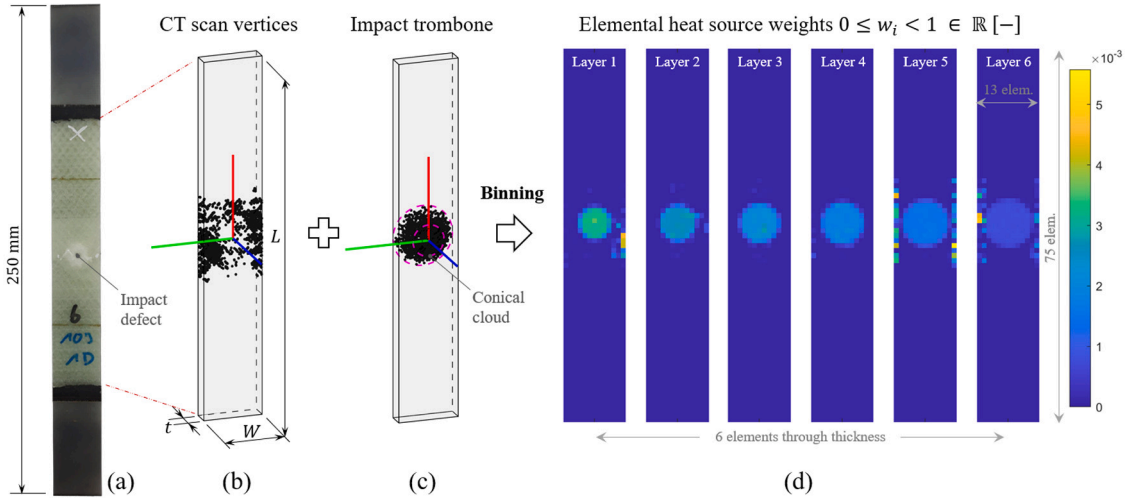

Fig. 2. (a) As impacted composite coupon with (b) binning the microcracks obtained from μ-CT in a cuboid domain (note: gauge length not to scale) and (c) binning the microcracks from a trombone shape point cloud sampled from a multivariate Gaussian distribution and (d) the resulting contour plots showing the weight distribution in each element separated for each layer.

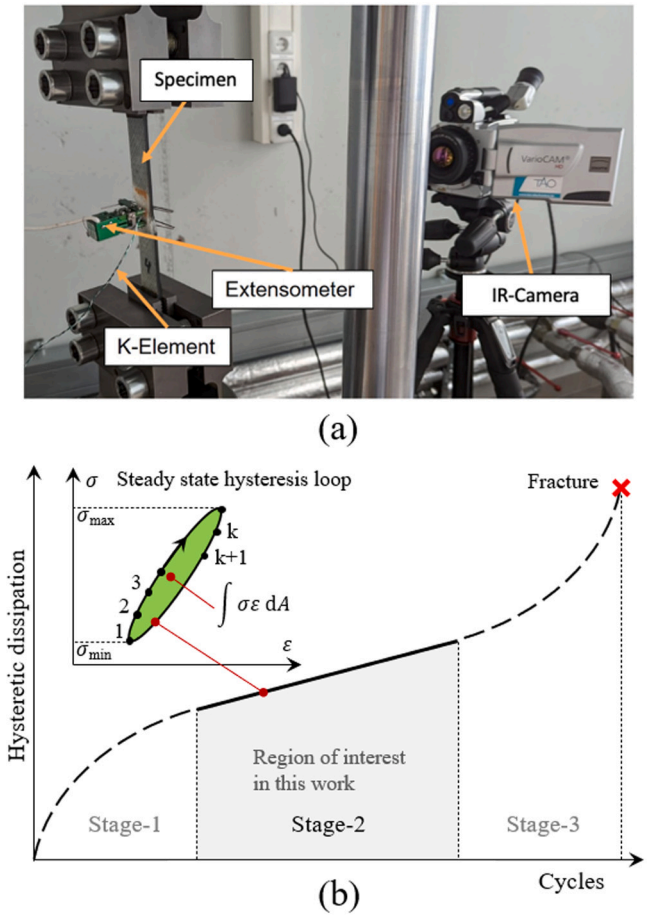

Fig. 3. (a) Tension-tension fatigue test set-up with installed coupon and thermal camera and (b) generic distribution of the dissipated energy over time where the focus of this investigation was on steady state (grey hatched region) exhibiting a small and constant change of the loop size. The inset depicts the numerical method to compute the hysteretic loss per cycle.

Algorithm 1 Binning algorithm

```
procedure BINNING(A, B, P, n)
    for i= 1 to 75 do
        for j = 1 to 13 do
            for k = 1 to 6 do
                A ← X_{i,j,k}                          ▷ elem. vertex coord.
                B ← X_{i+1,j+1,k+1}                    ▷ elem. vertex coord.
                P ← Point coord.
                find idx_1 ≥ A(1) and P(1) < B(1)
                find idx_2 ≥ A(2) and P(2) < B(2)
                find idx_3 ≤ A(3) and P(3) > B(3)
                find idx intersect(idx_1, idx_2, idx_3)
            end for
        end for
    end for
    return n ← P(idx)                                  ▷ points per element matrix
end procedure
```

$$\sum_{i=1}^{N} w_i = 1 \tag{3}$$

2.4. 3D FEM thermal analysis

Synthetic thermal images associated with the self-heating process of the pre-damaged specimens were generated by 3D thermal analysis of the free gauge length measured between the grips (cf. Fig. 4). The heat transfer model described by the partial differential equation for anisotropic conductivity and for internal heat generation can be written as follows:

$$\frac{\partial T}{\partial t} - \frac{1}{c_p \rho}\left(k_{xx}\frac{\partial^2 T}{\partial x^2} + k_{yy}\frac{\partial^2 T}{\partial y^2} + k_{zz}\frac{\partial^2 T}{\partial z^2}\right) = \frac{\sum \dot{q}_i}{c_p \rho} \tag{4}$$

where T is the temperature (in K), x, y, and z are Cartesian coordinates (in m), k_{ii} is the coefficient of thermal conductivity in i direction (in $\mathrm{W\,m^{-1}\,K^{-1}}$), $\dot{q}_i$ is the elemental heat influx (in W), c_p is the specific heat capacity (in $\mathrm{J\,K^{-1}\,kg^{-1}}$), and ρ is the material density (in $\mathrm{kg/m^3}$). The right hand side source term in Eq. (4) represents the intrinsic heat generated by the combination of viscoelastic damping and frictional damping in the impact region with the assumption that the energy is entirely converted into heat. The distribution and magnitude of heat generation in each element was reflected in the weights described in

Table 2
Thermal modelling parameters representing a generic orthotropic glass/epoxy fiber composite material used for all training images.

L m	W m	t m	ρ kg/m^3
0.15	0.025	0.006	1992.5
k_{xx} W/(mK)	$k_{yy} = k_{zz}$ W/(mK)	c_p J/(kgK)	T_0 K
0.805	0.374	940.5	293.15

the preceding section such that Eq. (5) holds.

$$\dot{q}_i = \dot{Q}\, w_i \tag{5}$$

In Eq. (5), $\dot{Q}$ (in W) is the total internal heat influx and w_i is the elemental unitless weight scalar. The thermal model simulated the *Stage-2* high cycle fatigue regime as indicated in Fig. 3(b). In this stage, the change of the hysteresis size between cycles is small and the coupon can be considered in thermal equilibrium at each instance where the IR image was taken. Therefore, with good approximation, the steady state solution of the heat transfer problem was considered for the synthetic thermal image i.e. $\partial T/\partial t \rightarrow 0$. Eq. (4) was numerically solved in its weak formulation within the framework of finite element analysis as described elsewhere [47,48].

2.4.1. Thermal boundary conditions

The contribution of radiative heat transfer $\propto T^4$ was neglected owing to the low temperature ranges involved. Conductive heat transfer boundary conditions were considered at both top and bottom end-surfaces assuming a negligible through-thickness temperature gradient at the ends. These conditions were modelled by assigning a steady state temperature corresponding to the surface temperature in the as-measured IR image. Natural convection occurs between the coupon and the cooler ambient air which is in contact with the coupon surfaces. In the thermal model, an averaged film coefficient was adopted such that the convective surface heat flux (q_{conv}, in W/m^2) takes the form $q_{\text{conv}} = \overline{h}\left(T_s - T_\infty\right)$, where $\overline{h} = 1/L \int_0^L h(x)\,\mathrm{d}x$. Here, h represents the average film coefficient for external surfaces (in W/(m^{2}K)), and T_s and T_∞ are the temperatures (in K) at the surface and in the surrounding ambient air, respectively.

The literature [49] provides empirical correlations for isothermal surfaces and some geometrical shapes assuming that the ambient air remote from the surface has zero velocity, notably

$$\frac{\overline{h}\,L}{k_{\text{air}}\left(T_f\right)} = \overline{\mathbf{Nu}} = C\,(\mathbf{Gr}\,\mathbf{Pr})^a \tag{6}$$

where $\overline{\mathbf{Nu}}$ is the average *Nusselt* number, k_{air} (in W/(mK)) is the coefficient of thermal conductivity of air, **Gr Pr** is the *Prandtl-Grashof* number, T_f is the temperature of the fluid (air) adjacent to the surface as indicated in Fig. 1(b) and a and C are empirical constants. This shows that obtaining the correct film coefficient using empirical approximations might lead to high levels of uncertainty since the coupon surface is not isothermal and **Gr Pr** in the laboratory environment is hard to determine. However, Eq. (6) has been used to determine the range of the film coefficient for the Bayesian optimization assuming laminar flow conditions in the convective film (no active cooling was used) with a *Prandtl-Grashof* number range of $1\times10^4 \leq \mathbf{Gr}\,\mathbf{Pr} \leq 1\times10^9$ cf. Fig. 1(b). Using a film temperature of $\left(T_s + T_\infty\right)/2 = 36\,^\circ$C, with the constants for a vertical plate $C = 0.59$, $a = 0.25$ and its equivalent length $L_v = 0.15$ m renders a film coefficient range of $1 \leq \overline{h} \leq 20$ W/m^{2}K. Table 2 lists the geometrical and thermal properties and the ambient temperature consistently adopted for the simulation of the training cases.

The commercial finite element software package *Comsol* [50] was used to solve the thermal model numerically. The *Comsol*-to-*Matlab* interface called *LiveLink* was used to build the thermal model and to discretize it with 5850 solid eight-noded elements and to read-in the weights w_i (cf. Eq. (2)) from a *.txt* file and to assign the corresponding elemental heat influx according to Eq. (5).

2.5. Bayesian optimization (BO)

The Bayesian optimization is a technique used to maximize or minimize specific target properties based on the corresponding features. It uses in general a gaussian processes (GP) model as regressor. The GP model is based on multivariate gaussian distributions, which generates one gaussian distribution per prediction, so that not only the predicted target property (or mean) is provided, but also its uncertainty (or standard deviation). GPs also use a kernel, which is an expression to quantify the similarity between any two samples. For instance, the radial basis function kernel is given by

$$k(\mathbf{x}, \mathbf{x}') = \exp\left(-\frac{|\mathbf{x} - \mathbf{x}'|^2}{2l^2}\right) \tag{7}$$

where $\mathbf{x}$ and $\mathbf{x}'$ represent input vectors or points in the input space and l is a hyperparameter that controls the rate at which the similarity decreases with distance. According to the GP model, samples exhibiting high similarity, as measured by the kernel value involving their features, also have very similar target properties.

The procedure of suggesting new experiments having maximized target properties starts with the generation of e.g. three initial random experiments, where each experiment is fully described by a vector of features. After these experiments are performed and the corresponding target property is measured, a (weak) GP model is trained with these data and sequentially used to perform predictions on a large number (e.g. 10^6) of virtual, randomly generated experiments. For each virtual experiment, the GP-generated prediction and related uncertainty are passed through an acquisition function, so that the final *utility* of all virtual experiments is computed. The maximum expected utility (EI) acquisition function is commonly used in Bayesian optimization and other optimization tasks, aiming to balance exploration and exploitation to efficiently locate the optimal solution in a computationally efficient manner. The EI function is given by:

$$\mathrm{EI}(\mathbf{x}) = \begin{cases} (\mu(\mathbf{x}) - f(\mathbf{x}^+) - \xi)\cdot \Phi(Z) + \ \sigma(\mathbf{x})\cdot\phi(Z) \\ \quad \text{if } \sigma(\mathbf{x}) > 0 \\ 0, \quad \text{otherwise} \end{cases} \tag{8}$$

where $\mu(\mathbf{x})$ represents the predictive mean of the GP model at input $\mathbf{x}$, $f(\mathbf{x}^+)$ is the best observed function value so far, and ξ is an exploration-exploitation trade-off parameter. Note that exploitation occurs when the value of the predicted target property is more important than its uncertainty, while exploration happens when the uncertainty is the dominant factor. $\Phi(Z)$ and $\phi(Z)$ represent the cumulative distribution function and probability density function, respectively, of the standard normal distribution evaluated at Z, while $\sigma(\mathbf{x})$ denotes the predictive standard deviation of the GP model at input $\mathbf{x}$. Z can be calculated by

$$Z = \frac{\mu(\mathbf{x}) - f(\mathbf{x}^+) - \xi}{\sigma(\mathbf{x})} \tag{9}$$

The virtual experiment with the maximum utility is then chosen to be performed in the laboratory, so that its corresponding target property is also measured. The next GP model will then have four samples and will gradually become more accurate. The BO cycles are repeated until the target property is high enough or whenever one decides to stop performing new measurements for any reason (e.g., little material available, high price of materials, long duration required for each experiment, etc.).

Two other techniques that are somehow related to BO are Active Learning (AL) and a full exploitation (here called “Greedy”). These two techniques can start by first training a (GP) model with the current dataset, then predicting the target property for all samples in a virtual

dataset. The virtual sample for which the highest uncertainty was obtained is suggested by AL (Note: AL can also select samples based on different criteria), which in this case represents a full exploration. On the other hand, the virtual sample with the highest predicted target property is suggested by the Greedy technique, therefore representing a full exploitation. If the target property is being minimized, then the Greedy technique suggests the parameters (or experiment) with the smallest target property.

2.6. Data treatment

All thermal images were first scaled to fit a resolution of 43 pixels (width) by 257 pixels (height) and had their pixel intensities, initially in the range from 0 to 255, converted to the absolute temperature scale using the available minimum and maximum temperatures. The similarity between the experimental and theoretical thermal images were quantified by the mean squared error loss function:

$$Loss = \frac{1}{n}\sum_{i=1}^{n}(y_i - \hat{y}_i)^2 \tag{10}$$

where n is the number of pixels in the image, and y_i and $\hat{y}_i$ are the true and predicted temperatures, respectively, for pixel i. The pixels occupied by the extensometer in the experimental images were excluded from the calculation of the loss function in Eq. (10).

2.7. Minimization of the target property

In this work, we started with few initial random vectors of ω, h and η, used as features in the dataset. Each such 3D vector corresponds to a FEM simulation, whose final output is one single thermal image. The similarity between each FEM image and the experimental one, as calculated by Eq. (10), was used as target property. BO rounds were then performed in order to propose new features from a virtual dataset with 10^6 samples, potentially exhibiting low target property (the negative of the target property was actually maximized). The BO rounds were intercalated either with AL, with the Greedy method or with a random drawing from the virtual dataset, as this strategy has been successfully adopted in a previous work [42].

Two distinct Bayesian optimization (BO) processes were conducted: one for the specimen impacted with 5 J of energy, and a separate one for the specimen impacted with 10 J of energy.

3. Results and discussion

3.1. Experimental results

Based on micro-computed tomography (μ-CT) measurements of the prepared laminates, 6 mm thick specimens exhibited delamination primarily within individual plies (see the SI). This behaviour is in contrast to thinner laminates, in which matrix cracking rather propagates throughout the volume. The observed behaviour in thick laminates can be attributed to their reduced flexibility and bending capacity, resulting in heightened local stress concentrations near the impact zone, ultimately leading to delamination, as shown in literature [30]. Therefore, a laminate thickness of 6 mm was chosen for subsequent testing due to the significance of self-heating effects in thicker laminates during fatigue loading and rather complex defect patterns observed in thin laminates.

The solid lines in Fig. 4(a–b) show the evolution of the measured dissipated power of the 5 J and 10 J test obtained from Eq. (1). The dissipated power is based on a constant amplitude stress range of 40 MPa, which, in a series of pre-trials, rendered a distinct thermal hotspot while simultaneously avoiding *Stage-3* growth. The red marker shows that the IR images were taken in a steady-state regime, where the hysteresis loop size was stabilized.

The experimental details related to the static shear tests, impact results, profilometer set up, and drop mass impact machine are shown in the SI.

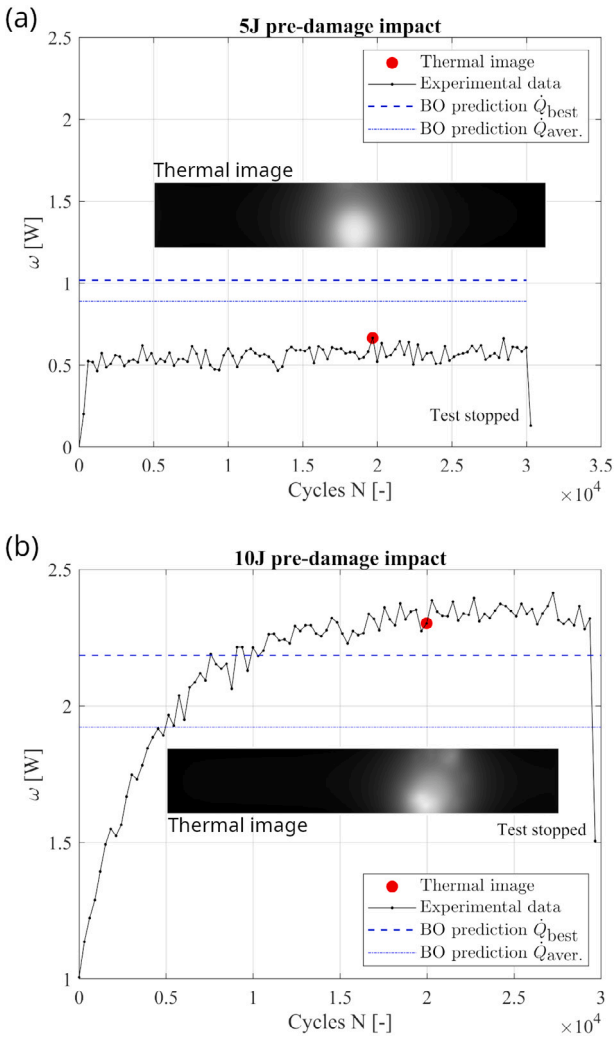

Fig. 4. Dissipated power in $J\,s^{-1}$ as a function of cycle number and corresponding optimal synthetic thermal image for (a) the 5 J test with $\eta = 0.443$, $h = 10.4\,W/m^2K$, $\dot{Q} = 1.018\,W$ and (b) the 10 J test with $\eta = 0.5$, $h = 20\,W/m^2K$, $\dot{Q} = 2.186\,W$.

3.2. Thermal analysis results

The synthetic thermal images embedded in Fig. 4(a–b) show the greyscale surface temperature field (the surface facing the thermal camera) predicted by the thermal model using the internal heat source distribution exemplary shown in Fig. 2(d). The synthetic thermal images are representing the optimized solution for the as-measured IR image taken at the indicated cycle number.

3.3. Optimized parameters

The evolution of the loss function (Eq. (10)) during the experiments is shown in Fig. 5 for both the 5 J and 10 J cases. The blue circles (BO rounds) gradually decreased the loss function and had in general smaller losses than the random or AL rounds, as indeed expected, as the random and AL points are used to improve the model. Note that Y axis of Fig. 5 uses logarithmic scale, as the second experiment in each pre-impact condition showed a relatively large loss.

Although the BO approach is well known to maximize or minimize target properties [42], the Greedy method also provided very small losses. The best sets of optimized FEM parameters obtained from Fig. 5 are provided in Table 3, which also shows the average value of these parameters out of the four lowest losses in each pre-impact case.

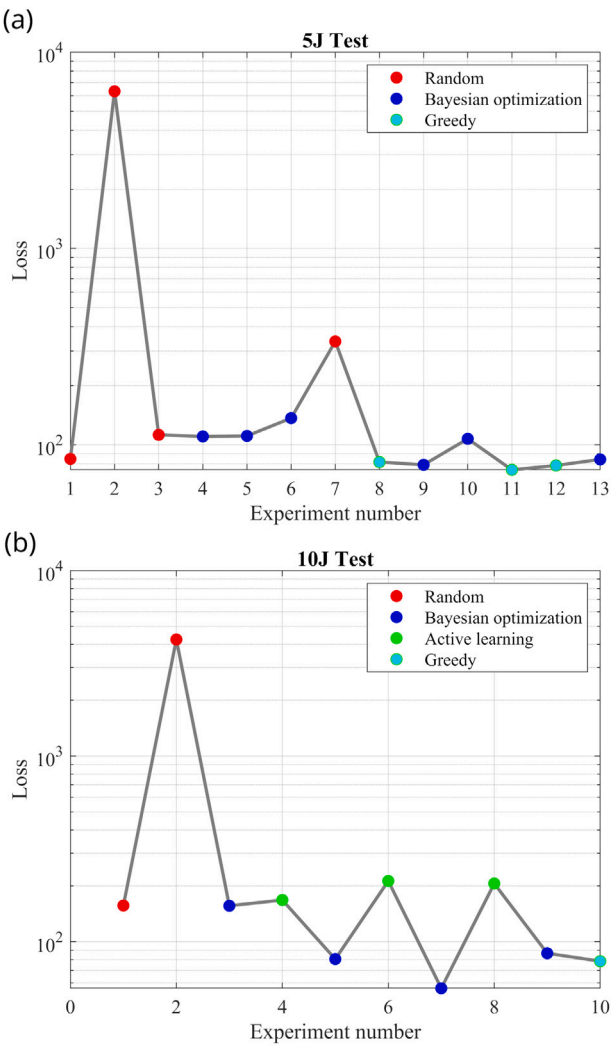

Fig. 5. The target property (*Loss*, Eq. (10)) as a function of the virtual experiment (or FEM simulation) number for (a) the 10 J and (b) the 5 J fatigue test. The BO, Greedy and AL techniques have been described in Section 2.5, while the Random technique is simply a random selection of one sample from a pool of 10^6 virtual samples.

The results in Table 3 show that the film coefficient exhibits a high sensitivity in the self-heating problem of composite coupons and its influence should be considered in the thermal analysis of IR imaging. The variation of the predicted film coefficient between the two tests was considerable although the surface roughness and local airflow conditions prevailing during the tests were similar. However, the film coefficient in the investigated cases was found to vary between $10\,\mathrm{W/m^2K}$ to $20\,\mathrm{W/m^2K}$, which corresponds to a *Reynolds* number range of 1×10^8 to 1×10^9 representing laminar flow conditions.

The latter are consistent with the laboratory testing conditions which did not rely on active cooling e.g. ventilators or local air-suction. Moreover, the predicted film coefficients agree with the range proposed by Huang et al. [51]. Similar values were used by Ignatova and Sapozhnikov et al. in their studies predicting self-heating mechanism of GFRP under fatigue bending conditions [52,53].

The lowest losses obtained for specimens with 5 J and 10 J impacts were experiments #11 (Fig. 5(a) and #7 (Fig. 5(b), respectively. The artificial (FEM) thermal images originated from these two experiments are compared with the corresponding experimental images in Fig. 6. The comparison of the predicted total work loss with the as-measured values in Table 3 shows that the accuracy achieved for the 10 J coupon was higher than that of the 5 J coupon. Given the considerable level

Table 3
Optimized parameters $\dot{Q}$ (in W), h (in $\mathrm{W/m^2}$) and the unitless η at minimal loss and weighted average of the best four points compared with the measured dissipated power ω (in W) for the 5 J and 10 J fatigue tests; relative error in %.

Case	$\dot{Q}$	ω	h	η	$100\,(\dot{Q}-\omega)\,/\omega$
5J Best[a]	1.02	0.66	10.5	0.44	54
5J Avg.[b]	0.89	0.66	10.1	0.43	35
10J Best[c]	2.19	2.3	20.0	0.50	−5
10J Avg.[d]	1.92	2.3	19.3	0.44	−16

Experiment #:
[a] 11.
[b] 8, 9, 11, 12.
[c] 7.
[d] 5, 7, 9, 10.

of experimental- and modelling uncertainty it can be concluded that the agreement between the predicted and experimentally obtained dissipated energy ranges between good and reasonable.

The average viscoelastic dissipation factor predicted by BO is $\eta_{\mathrm{pred}} = 0.45$, which agrees reasonably well with the measured average experimental dissipation of $\eta_{\mathrm{exp}} = 0.42$. From this, it can be inferred that in the presented case, approximately 40%–50% of the total energy was dissipated by viscoelastic effects.

It is important to note that this estimation relies on the assumption of uniform viscoelastic dissipation, while neglecting other potential localized and complementary dissipative mechanisms, including molecular bond breakage and thermoelastic effects, among others. In this work, this simplification clearly represents a coarse approximation of the real physics, and further investigations may be required to account for the intricacies of these additional dissipative mechanisms.

4. Conclusion

It can be concluded from the results that passive thermography when applied in conjunction with BO and thermal modelling can provide physically meaningful key parameters mathematically defining the self-heating PDE problem inside fiber/polymer composite materials during high cycle fatigue testing. Inferring from the convergence behaviour of the predictions, BO can be considered an efficient means to optimize a multidimensional parameter space in thermal analysis problems — which in the present case only required 10–13 virtual experiments (i.e. FEA runs) to achieve an acceptably small loss. The results show that synthetic thermal images obtained from numerical thermal analysis can indeed be used for ML as a supplement to real thermographic images. This represents a major insight and advantage inasmuch synthetic thermal images can be generated at a fraction of the cost and time required to obtain experimentally measured thermal images for training purposes. The determination of the key parameters within more narrow value ranges through BO will improve the accuracy and quality of the synthetic thermal images which consequently will enhance the ML training process. Furthermore, the proposed BO technique can provide information encoded in the thermal image which cannot be obtained by direct measurements otherwise. This holds particularly true for the film coefficient and for the viscous damping contribution. To optimize the key parameters, synthetic thermal surface images were generated through numerical thermal analysis (FEA) using randomly selected key parameter values from predefined physically meaningful ranges. BO rounds were performed on the basis of the synthetic images by iteratively proposing new parameter sets for the FEA runs whilst minimizing the loss between the synthetic image and the experimental image. These BO rounds alternated between active learning, greedy learning, and random drawing strategies, until the loss reached a stable minimum.

In the sequence of the key parameters defined in the introduction, the following can be inferred from the results and further explicated:

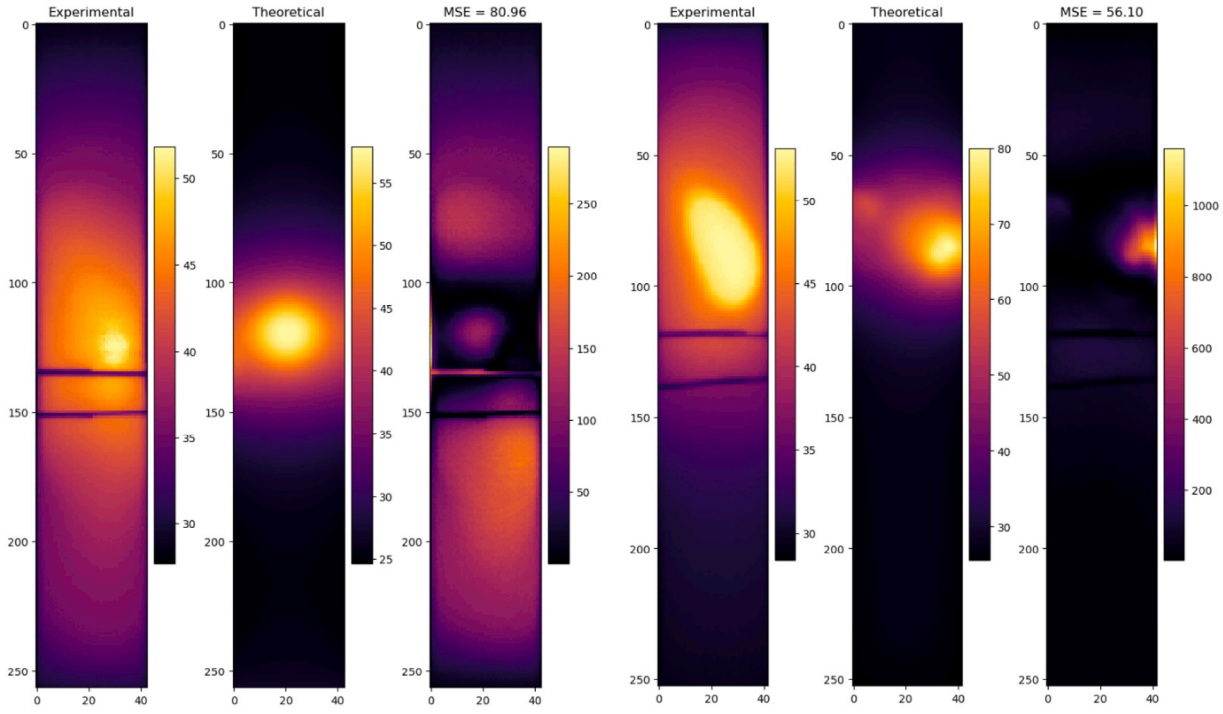

(a) 5 J coupon (b) 10 J coupon

Fig. 6. As-measured IR image (left), synthetic thermal image (middle) and loss contours (right) shown for the optimal experiment for (a) the 5 J pre-impact coupon and (b) the 10 J pre-impact coupon. The scale bars show temperature values in °C.

1. The film coefficient ranges predicted in the investigated cases correspond to laminar air flow conditions consistent with the laboratory testing conditions. Furthermore, the predicted coefficient is in reasonable agreement with values reported in the literature.
2. The agreement between the predicted and measured work loss for the 5 J and the 10 J test was good given the significant experimental and modelling uncertainties.
3. The predicted range for the average viscoelastic dissipation factor, spanning from 40% to 50%, exhibits a reasonable agreement with the experimentally measured average dissipation obtained from benchmark tests on intact coupons.

Future work: The computationally most expensive part of the BO rounds was the automatic FE-model generation from the heat source data and solving the thermal problem. Future research effort will be dedicated to increase the efficiency of the synthetic thermal image generation through a complimentary ML model. Despite the possibility to determine more accurate parameter values by finding the absolute minima, this endeavor is considered beyond the scope of this investigation and will also be addressed in future developments.

CRediT authorship contribution statement

Martin Demleitner: Investigation, Methodology, Validation, Writing – original draft, Writing – review & editing. **Rodrigo Q. Albuquerque:** Conceptualization, Investigation, Methodology, Software, Writing – original draft, Writing – review & editing. **Ali Sarhadi:** Formal analysis, Investigation, Methodology, Software, Writing – original draft, Writing – review & editing. **Holger Ruckdäschel:** Funding acquisition, Resources, Writing – review & editing. **Martin A. Eder:** Conceptualization, Formal analysis, Investigation, Methodology, Project administration, Software, Writing – original draft, Writing – review & editing.

Declaration of competing interest

The authors declare the following financial interests/personal relationships which may be considered as potential competing interests: Rodrigo Q. Albuquerque reports financial support was provided by Bayerischen Staatsministerium für Wissenschaft und Kunst.

Data availability

Data will be made available on request.

Acknowledgements

This publication was funded by the University of Bayreuth in the funding program Open Access Publishing. Parts of this work were funded by the "Bayerischen Staatsministerium für Wissenschaft und Kunst" (grant # F.2-M7426.10.2. 1/4/16, Germany). DTU Wind and Energy Systems is grateful for the financial support of this publication by VILLUM FONDEN with grant number 36050. Furthermore, DTU Wind and Energy Systems acknowledges the financial support through the EUDP project ReliaBlade with grant number 64018-0068. We would like to thank Mr. Alexander Brückner of the University of Bayreuth for carrying out the dynamic fatigue testing and Dr. Birgit Striegl of the OTH Regensburg for carrying out the μ-CT measurements.

Appendix A. Supplementary data

Supplementary material related to this article can be found online at https://doi.org/10.1016/j.compscitech.2024.110439.

References

[1] Xiao Chen, Martin A. Eder, A.S.M. Shihavuddin, Dan Zheng, A human-cyber-physical system toward intelligent wind turbine operation and maintenance, Sustainability (Switzerland) (2021).

[2] Max Spencer, Shohreh Sheiati, Xiao Chen, AQUADA GUI: A graphical user interface for automated quantification of damages in composite structures under fatigue loading using computer vision and thermography, Softwarex 22 (2023) 101392.

[3] Xiao Chen, Shohreh Sheiati, A.S.M. Shihavuddin, AQUADA PLUS: Automated damage inspection of cyclic-loaded large-scale composite structures using thermal imagery and computer vision, Compos. Struct. 318 (2023) 117085.

[4] Aravind Premanand, Tomasz Rogala, Dominik Wachla, Jafar Amraei, Andrzej Katunin, Bilal Khatri, Michael Rienks, Frank Balle, Fatigue strength estimation of a CF/PEKK composite through self-heating temperature analysis using cyclic bending tests at 20 khz, Compos. Sci. Technol. 243 (2023) 110218.

[5] Jafar Amraei, Andrzej Katunin, Recent advances in limiting fatigue damage accumulation induced by self-heating in polymer-matrix composites, Polymers 14 (24) (2022).

[6] Martin A. Eder, Ali Sarhadi, Xiao Chen, A novel and robust method to quantify fatigue damage in fibre composite materials using thermal imaging analysis, Int. J. Fatigue 150 (2021) 106326.

[7] Xiao Chen, Rims Janeliukstis, Ali Sarhadi, Thermographic data analytics-based damage characterization in a large-scale composite structure under cyclic loading, Compos. Struct. 290 (2022) 115525.

[8] Jefri Bale, Emmanuel Valot, Olivier Polit, Claude Bathias, Martine Monin, Tresna Soemardi, Thermal phenomenon of glass fibre composite under tensile static and fatigue loading, J. Mech. Eng. Sci. 11 (2) (2017) 2755–2769.

[9] J.E. Thatcher, D.A. Crump, C. Devivier, P.B.S. Bailey, J.M. Dulieu-Barton, Low cost infrared thermography for automated crack monitoring in fatigue testing, Opt. Lasers Eng. 126 (2020) 105914.

[10] A. Katunin, Evaluation of criticality of self-heating of polymer composites by estimating the heat dissipation rate, Mech. Compos. Mater. 54 (1) (2018) 53–60.

[11] Ali Mahmoudi, B. Mohammadi, Theoretical-experimental investigation of temperature evolution in laminated composites due to fatigue loading, Compos. Struct. 225 (2019) 110972.

[12] A.H. Mirzaei, M.M. Shokrieh, Simulation and measurement of the self-heating phenomenon of carbon/epoxy laminated composites under fatigue loading, Composites B 223 (2021) 109097.

[13] R. Steinberger, T.I. Valadas Leitão, E. Ladstätter, G. Pinter, W. Billinger, R.W. Lang, Infrared thermographic techniques for non-destructive damage characterization of carbon fibre reinforced polymers during tensile fatigue testing, Int. J. Fatigue 28 (10) (2006) 1340–1347.

[14] Francisco Lahuerta, Rogier P.L. Nijssen, Energy dissipation in thermoset composites in mode I fatigue, vol. 24, no. 2, 2016, pp. 168–175, http://dx.doi.org/10.1080/15376494.2015.1124950.

[15] Abderrahmane Djabali, Lotfi Toubal, Redouane Zitoune, Saïd Rechak, Fatigue damage evolution in thick composite laminates: Combination of X-ray tomography, acoustic emission and digital image correlation, Compos. Sci. Technol. 183 (2019) 107815.

[16] Sachin S. Pawar, Kara Peters, Through-the-thickness identification of impact damage in composite laminates through pulsed phase thermography, Meas. Sci. Technol. 24 (11) (2013) 115601.

[17] Henrik Schmutzler, Marko Alder, Nils Kosmann, Hans Wittich, Karl Schulte, Degradation monitoring of impact damaged carbon fibre reinforced polymers under fatigue loading with pulse phase thermography, Composites B 59 (2014) 221–229.

[18] N. Kosmann, B.T. Riecken, H. Schmutzler, J.B. Knoll, K. Schulte, B. Fiedler, Evaluation of a critical impact energy in GFRP under fatigue loading, Compos. Sci. Technol. 102 (2014) 28–34.

[19] Hongliang Tuo, Tao Wu, Zhixian Lu, Xiaoping Ma, Evaluation of damage evolution of impacted composite laminates under fatigue loadings by infrared thermography and ultrasonic methods, Polym. Test. 93 (2021) 106869.

[20] A. Quinlan, O. Castro, J.M. Dulieu-Barton, Towards assessment of fatigue damage in composite laminates using thermoelastic stress analysis, Composites C 12 (2023) 100377.

[21] Colin Robert, Toa Pecur, James M. Maguire, Austin D. Lafferty, Edward D. McCarthy, Conchúr M.Ó. Brádaigh, A novel powder-epoxy towpregging line for wind and tidal turbine blades, Composites B 203 (2020) 108443.

[22] James M. Maguire, Kapileswar Nayak, M. Ó Brádaigh, Novel epoxy powder for manufacturing thick-section composite parts under vacuum-bag-only conditions. Part II: Experimental validation and process investigations, 2020, http://dx.doi.org/10.1016/j.compositesa.2020.105970.

[23] Zhang Lanting, Energy procedia energy procedia 00 (2011) 000-000 www.elsevier.com/locate/procedia research on structural lay-up optimum design of composite wind turbine blade peer-review under responsibility of [name organizer], Energy Procedia 14 (2012) 637–642.

[24] F. Lahuerta, R.P.L. Nijssen, F.P. Van Der Meer, L.J. Sluys, Static and Dynamic Through Thickness Lamina Properties of Thick Laminates, Proceedings of the 20th International Conference on Composite Materials (ICCM 20), Copenhagen, Denmark, 19-24 July 2015, DOI: http://resolver.tudelft.nl/uuid:56bdc196-9322-48d5-a272-1b7aa2fb04b5.

[25] Benedikt Kötter, Janina Endres, Johann Körbelin, Florian Bittner, Hans Josef Endres, Bodo Fiedler, Fatigue and fatigue after impact behaviour of Thin- and Thick-Ply composites observed by computed tomography, Composites C 5 (2021) 100139.

[26] H. Hamidi, W. Xiong, S.V. Hoa, R. Ganesan, Fatigue behavior of thick composite laminates under flexural loading, 2018, http://dx.doi.org/10.1016/j.compstruct.2018.05.149.

[27] Rajamohan Ganesan, Fatigue behavior of thick composite laminates, Fatigue Life Predict. Compos. Compos. Struct. (2020) 239–267.

[28] S. Gul, I.E. Tabrizi, B.S. Okan, A. Kefal, M. Yildiz, An experimental investigation on damage mechanisms of thick hybrid composite structures under flexural loading using multi-instrument measurements, Aerosp. Sci. Technol. 117 (2021) 106921.

[29] Abderrahmane Djabali, Lotfi Toubal, Redouane Zitoune, Saïd Rechak, An experimental investigation of the mechanical behavior and damage of thick laminated carbon/epoxy composite, Compos. Struct. 184 (2018) 178–190.

[30] Rohchoon Park, Jyongsik Jang, Effect of laminate thickness on impact behavior of aramid fiber/vinylester composites, Polym. Test. 22 (8) (2003) 939–946.

[31] Aizhou Chen, Yuan Li, Bo Yan, Computational inverse methods of heat source in fatigue damage problems, in: AIP Conference Proceedings, 2018.

[32] Jingbo Wang, Nicholas Zabaras, A Bayesian inference approach to the inverse heat conduction problem, Int. J. Heat Mass Transfer 47 (17–18) (2004) 3927–3941.

[33] Mattia Bergagio, Haipeng Li, Henryk Anglart, An iterative finite-element algorithm for solving two-dimensional nonlinear inverse heat conduction problems, 2018, http://dx.doi.org/10.1016/j.ijheatmasstransfer.2018.04.104.

[34] S. Ardabili, A. Mosavi, I. Felde, Machine Learning in Heat Transfer: Taxonomy, Review and Evaluation, in: SACI 2023 - IEEE 17th International Symposium on Applied Computational Intelligence and Informatics, Proceedings, Institute of Electrical and Electronics Engineers Inc., 2023, pp. 433–441.

[35] Numan Saeed, Mohammed A. Omar, Yusra Abdulrahman, A neural network approach for quantifying defects depth, for nondestructive testing thermograms, Infrared Phys. Technol. 94 (2018) 55–64.

[36] Akbar Darabi, Xavier Maldague, Neural network based defect detection and depth estimation in TNDE, NDT & E Int. 35 (3) (2002) 165–175.

[37] Kaixin Liu, Qing Yu, Yi Liu, Jianguo Yang, Yuan Yao, Convolutional graph thermography for subsurface defect detection in polymer composites, IEEE Trans. Instrum. Meas. 71 (2022).

[38] Qin Luo, Bin Gao, W.L. Woo, Yang Yang, Temporal and spatial deep learning network for infrared thermal defect detection, NDT & E Int. 108 (2019) 102164.

[39] Sirawit Pruksawan, Guillaume Lambard, Sadaki Samitsu, Keitaro Sodeyama, Masanobu Naito, Prediction and optimization of epoxy adhesive strength from a small dataset through active learning, Sci. Technol. Adv. Mater. 20 (1) (2019) 1010–1021, PMID: 31692965.

[40] James R. Deneault, Jorge Chang, Jay Myung, Daylond Hooper, Andrew Armstrong, Mark Pitt, Benji Maruyama, Toward autonomous additive manufacturing: Bayesian optimization on a 3D printer, MRS Bull. 46 (7) (2021) 566–575.

[41] Kundo Park, Youngsoo Kim, Minki Kim, Chihyeon Song, Jinkyoo Park, Seunghwa Ryu, Designing staggered platelet composite structure with Gaussian process regression based Bayesian optimization, Compos. Sci. Technol. 220 (2022) 109254.

[42] Rodrigo Q. Albuquerque, Florian Rothenhäusler, Holger Ruckdäschel, Designing formulations of bio-based, multicomponent epoxy resin systems via machine learning, MRS Bull. (2023) http://dx.doi.org/10.1557/s43577-023-00504-9.

[43] Fengqing Chen, Zhen Guo, Jinhe Wang, Runhai Ouyang, Dianpu Ma, Pei Gao, Fei Pan, Peng Ding, Accelerated feasible screening of flame-retardant polymeric composites using data-driven multi-objective optimization, Comput. Mater. Sci. 230 (2023) 112479.

[44] Kianoosh Sattari, Yunchao Xie, Jian Lin, Data-driven algorithms for inverse design of polymers, Soft Matter 17 (2021) 7607–7622.

[45] Fibre-reinforced plastic composites —- Determination of the in-plane shear stress/shear strain response, including the in-plane shear modulus and strength, by the plus or minus 45 degree tension test method, vol. 2000, ISO/TC 61/SC 13 Composites and reinforcement fibres, Geneva, CH, 1997, ISO 14129:1997.

[46] MATLAB 2021, Documentation, version 7.10.0 (r2020a), Natick, Massachusetts: The MathWorks inc., 2021, version 7.10.0 (R2020a), Natick, Massachusetts: The MathWorks Inc.

[47] Ali Sarhadi, Jesper Henri Hattel, Hans Nørgaard Hansen, Cem Celal Tutum, Lasse Lorenzen, Peter M.W. Skovgaard, Thermal modelling of the multi-stage heating system with variable boundary conditions in the wafer based precision glass moulding process, J. Mater Process. Technol. 212 (8) (2012) 1771–1779.

[48] Ali Sarhadi, Jesper Henri Hattel, Hans Nørgaard Hansen, Cem Celal Tutum, Numerical modeling of the conduction and radiation heating in precision glass moulding, in: Proceedings of the 12th Euspen International Conference, 2012.

[49] George Sidebotham, Heat Transfer Modeling : An Inductive Approach, Springer, 2015, xviii, 516 Seiten (unknown).

[50] COMSOL Inc., COMSOL, 2020.
[51] Jia Huang, Christian Garnier, Marie Laetitia Pastor, Xiaojing Gong, Investigation of self-heating and life prediction in CFRP laminates under cyclic shear loading condition based on the infrared thermographic data, Eng. Fract. Mech. 229 (2020).
[52] A.V. Ignatova, A.V. Bezmelnitsyn, N.A. Olivenko, O.A. Kudryavtsev, S.B. Sapozhnikov, A.D. Shavshina, Prediction of GFRP self-heating kinetics under cyclic bending, Mech. Compos. Mater. 58 (6) (2023) 787–802.
[53] S.B. Sapozhnikov, A.A. Shabley, A.V. Ignatova, Predicting the kinetics of hysteretic self-heating of GFRPs under high-frequency cyclic loading, Compos. Struct. 226 (2019) 111214.